# Vorticity of polariton condensates in rotating traps

A. V. Yulin,[1,2] I. A. Shelykh,[1,2,3] E. S. Sedov,[4,5,6] and A. V. Kavokin[2,5,7,8]
[1]*Department of Physics, ITMO University, Saint Petersburg 197101, Russia*
[2]*Abrikosov Center for Theoretical Physics, MIPT, Dolgoprudnyi, Moscow Region 141701, Russia*
[3]*Science Institute, University of Iceland, Dunhagi 3, IS-107 Reykjavik, Iceland*
[4]*Russian Quantum Center, Skolkovo Innovation Center, Moscow 121205, Russia*
[5]*Spin-Optics Laboratory, St. Petersburg State University, St. Petersburg 198504, Russia*
[6]*Vladimir State University, Vladimir 600000, Russia*
[7]*Westlake University, School of Science, 18 Shilongshan Road, Hangzhou 310024, Zhejiang Province, China*
[8]*Westlake Institute for Advanced Study, Institute of Natural Sciences, 18 Shilongshan Road, Hangzhou 310024, Zhejiang Province, China*

(Received 5 July 2023; accepted 15 September 2023; published 3 October 2023)

This work is inspired by recent experiments on the formation of vortices in exciton-polariton condensates placed in rotating optical traps. We study theoretically the dynamics of the formation of such vortices and elucidate the fundamental role of the mode competition effect in determining the properties of stationary polariton states triggered by stimulated scattering of exciton-polaritons. The interplay between linear and nonlinear effects is shown to result in peculiar polariton dynamics. However, near the lasing threshold, the predominant contribution of the nonlinear effects is the saturation of the linear gain.

DOI: 10.1103/PhysRevB.108.155301

## I. INTRODUCTION

Semiconductor systems suitable for the realization of strong light-matter coupling have been actively studied in recent years [1]. The reason for the interest they attract is the hybridization between the cavity photons and electronic excitations, which gives rise to the appearance of quasiparticles having extremely low effective masses and being able to efficiently interact with each other. Probably the most remarkable achievement in this field is the experimental realization of Bose-Einstein condensation of exciton polaritons at extraordinarily high temperatures [2,3]. This fundamental discovery paved the way for the practical realization of polariton lasers [4–6].

Coherent ensembles of interacting polaritons reveal the phenomenon of superfluidity [1], and in certain geometries, polariton states sustaining persistent currents may be formed [7–16]. The corresponding nonlinear localized structures characterized by a topological charge, known as polariton vortices, have been extensively studied from both theoretical and experimental perspectives [16–20].

States of the opposite vorticity can form the basis of a polariton qubit [21,22]. It is therefore important to possess a tool to have control over the direction of the polariton rotation. This can be achieved by using chiral structures [23,24], fine tuning the excitation conditions [25], using the effect of spin to angular momentum conversion [26], using Laguerre-Gaussian beams [27], or applying external magnetic fields [28].

The study of mesoscopic coherent polariton states, including vortices, confined in the microcavity plane using potential traps has attracted considerable interest [29–36]. Particularly noteworthy are annular optical traps, which can be induced in the microcavity by laser beams with appropriate spatial profiles [33–36]. It was recently shown that the formation of an external rotating potential is a powerful tool for controlling the polariton states forming in annular traps [37,38]. The goal of this paper is to provide a theoretical analysis of the dynamics of the polariton condensates in these geometries in the vicinity of a polariton lasing threshold and to elucidate the mechanism responsible for the symmetry breaking between the clockwise and counterclockwise rotating solutions. We consider two distinct experimentally relevant situations, corresponding to three different coupling schemes between the states of distinct vorticities induced by the rotating potential. Vorticity is characterized by the angular index $m$, which quantifies the number of times the phase of a wave winds as one moves around the vortex core. Namely, we analyze the cases of the coupling between $m = 0$ and $\pm 1$ states, the coupling between $m = \pm 1$ and $\pm 2$ states, and the coupling between $m = -1$ and $+1$ states [37].

The formation of polariton vortices in a trap with a rotating complex potential is considered within the framework of the generalized scalar Gross-Pitaevskii equation. It is shown that close to the polariton lasing threshold, the stationary states inherit their angular momentum from the fastest growing linear mode. In fact, during the linear stage of condensation at the beginning of the polariton evolution, the polariton field can be expressed as a combination of different eigenmodes. Because the condensation process originates from an incoherent exciton reservoir, the eigenfrequencies of these modes are complex, with some modes exhibiting exponential growth over time. The mode with the highest growth rate, at a certain point, suppresses the other modes and consequently shapes the structure of the stationary condensate.

It is worth noting that in the presence of the azimuth nonsymmetric potential, the polariton eigenmodes can be expressed as a combination of multiple components with

 ©2023 American Physical Society

different angular indices [13,14]. The resulting direction of rotation of the polariton state is determined by the relative weights associated with these components. These weights, in turn, are influenced by the angular velocity of the rotating potential. At certain threshold angular velocities, the velocity of the condensate can cross zero and undergo a change in sign.

There is an additional scenario that can lead to a change in the rotation velocity of the condensate. This scenario arises from a swap between the fastest and the second fastest growing modes. In the case considered in the paper, polaritons in these modes rotate in different directions, with not only different absolute values of velocities but also opposite signs. Therefore, if the fastest and the second fastest modes swap at a certain velocity, the rotation direction of the stationary polaritons also changes. In this scenario, the velocity of the polariton rotation is not a continuous function of the rotating potential velocity. Instead, it undergoes a distinct change by a finite value at critical velocities of the potential. To analytically describe the observed effects, a perturbation approach was employed. The developed coupled mode theory effectively reproduces the results obtained from direct two-dimensional (2D) simulations.

The paper is organized as follows. After the Introduction, in Sec. II, we describe the considered geometry and introduce the corresponding mathematical model. In the third section, we provide a brief discussion of the formation of hybrid states in the presence of the rotating potential that couples modes with different angular indices. Section IV contains the numerical results concerning the hybridization of the modes with an angular index difference equal to 1. The perturbation theory explaining the numerical results is developed in the fifth section. Various mechanisms governing the formation of stationary polariton states in the rotating potentials are discussed in Sec. VI. Finally, in the Conclusion, we briefly summarize the main findings of the paper.

## II. THE SYSTEM IN QUESTION AND ITS MATHEMATICAL DESCRIPTION

We consider the geometry of an annular trap created by an axially symmetric incoherent pump, which produces both the conservative confining potential for a condensate due to the effect of reservoir-induced blueshift and the effective linear gain provided by the stimulated condensation of polaritons from a reservoir to a coherent state. We also account for the axially symmetric conservative potential created by the microstructuring of a sample. We opted to incorporate this potential for two primary reasons. The first reason is that this potential contributes to the confinement of polaritons, thereby enhancing the suitability of the coupled mode approach developed to elucidate the phenomena observed in numerical simulations. The second reason is of a technical nature: The supplementary conservative potential facilitates control over the condensate properties. A schematic representation of the excitation and trapping of the polariton condensate is shown in Fig. 1(a).

Control of vorticity is achieved via an additional rotating nonresonant pump, which can be created by the application of two interfering optical beams with different orbital angular momenta (Laguerre-Gaussian modes) and slightly detuned

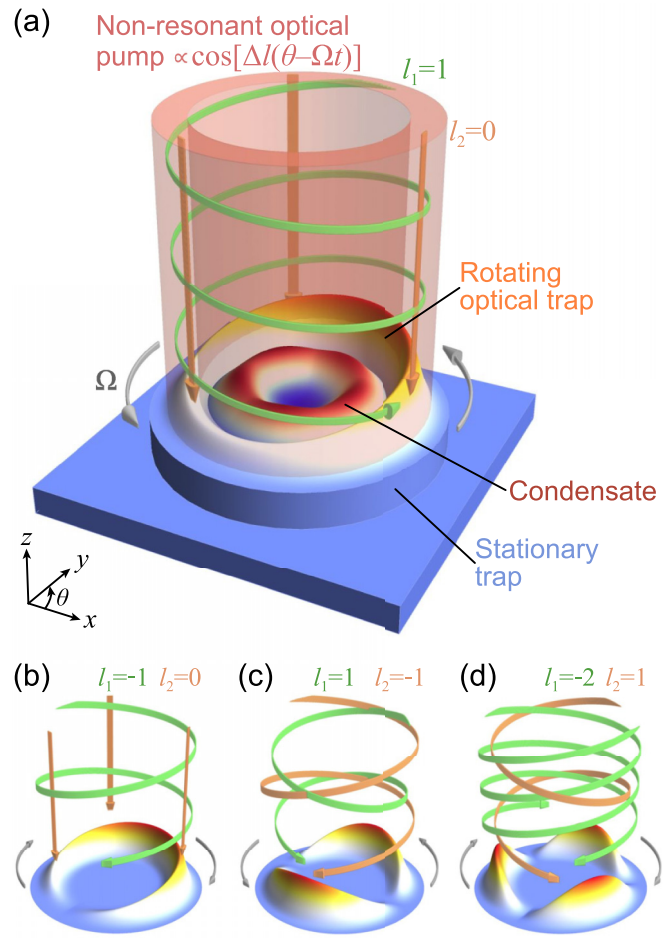


FIG. 1. (a) Schematic depicting the excitation of a polariton condensate in an external rotating optical potential. The rotation is induced by two laser beams with angular momenta $l_1 = 1$ and $l_2 = 0$, characterized by different frequencies $\Omega = \omega_1 - \omega_2$. (b)–(d) The shape of the rotating part of the pump-induced optical trap depending on the angular momenta of the optical pump components. The frequencies in the panels are taken as $\omega_1 > \omega_2$.

frequencies, and thus reads

$$P_r(\mathbf{r}, t) = \tilde{f}(r)\cos[\Delta l(\theta - \Omega t)], \tag{1}$$

where $\tilde{f}(r)$ describes the radial dependence of the pump, $\Delta l = l_1 - l_2$ denotes the difference in the angular indices between the beams creating the pump, $\Omega = \omega_1 - \omega_2$ is the rotation velocity of the potential defined by the detuning between the two pumping modes, and $r$ and $\theta$ correspond to the radial and angular coordinates, respectively. Indices 1 and 2 enumerate the interfering beams. In panels (b)–(d) of Fig. 1, we show schematically examples of the rotating potentials created by two beams with different combinations of $l_1$ and $l_2$. We assume $\omega_1 > \omega_2$ for definiteness. The absolute value of the difference $\Delta l$ determines the number of variations of the potential in the azimuthal direction, while its sign determines the direction of rotation of the potential. It is worth noting that when $\omega_1 < \omega_2$, the rotation direction of the potential trap is reversed.

Let us stress once more that the rotating pump results in both the rotating conservative potential and the rotating gain for the condensate, as will become clear from the dynamic equations that we introduce below.

In the scalar case, the problem can be described by the equations that govern the polariton condensate, characterized by the order parameter function $\Psi(\mathbf{r},t)$ and the density of the incoherent exciton reservoir $\rho(\mathbf{r},t)$:

$$i\hbar\partial_t\Psi = \frac{\hbar^2}{2m^*}\nabla^2\Psi - [\tilde{V}(r) + i\hbar\Gamma_p + \hbar(g_2 - ig_1)\rho]\Psi - (H + i\tilde{H})|\Psi|^2\Psi, \tag{2a}$$

$$\partial_t\rho = -(\Gamma_r + 2g_1|\Psi|^2)\rho + P(\mathbf{r},t), \tag{2b}$$

where $m^*$ is the effective mass of polaritons in the microcavity plane, $\tilde{V}(r)$ is the axially symmetric conservative potential created by the microstructuring, and the term $\hbar\Gamma_p\Psi$ accounts for the intrinsic losses in the cavity that we assume to be spatially uniform. The coefficient $g_1$ is the rate of the stimulated scattering of reservoir excitons into the coherent polariton state, and the coefficient $g_2$ defines the reservoir-induced blueshift of the condensate as a function of its density. The nonlinear self-induced blueshift of the coherent polariton state is described by the parameter $H$, and the coefficient $\tilde{H}$ accounts for the nonlinear losses of coherent polaritons. Finally, $\Gamma_r$ is the relaxation rate of the incoherent reservoir excitons. The total incoherent pump is accounted for by $P(\mathbf{r},t)$ standing on the right-hand side of Eq. (2b). The pump $P(\mathbf{r},t) = P_0(r) + P_r(\mathbf{r},t)$ contains two components, including the time-independent axially symmetric term $P_0(r)$ and the rotating term $P_r(\mathbf{r},t)$ defined by Eq. (1). It is noteworthy that the problem of vortex formation in polariton condensates created solely by the rotating pump is of significant interest. However, it requires specific examination and, as such, falls beyond the scope of the current paper.

Let us assume that the relaxation of incoherent excitons is fast compared to other characteristic timescales of polariton dynamics. This allows us to adiabatically eliminate $\rho$ setting $\partial_t\rho = 0$ and thus obtain the following equation for the macroscopic wave function of the condensate. Introducing the dimensionless time $t \to t/2\Gamma_p$, the coordinate $x \to x\sqrt{\hbar/2m^*\Gamma_p}$, and the order parameter function $\psi = \Psi\sqrt{2g_1/\Gamma_r}$, we get

$$i\partial_t\psi = \frac{1}{2}\nabla^2\psi - \left(V + \frac{i}{2}\right)\psi - (1 - i\alpha)\frac{W_0 + W_r}{1 + |\psi|^2}\psi - (h + i\tilde{h})|\psi|^2\psi, \tag{3}$$

where $V = \tilde{V}/2\hbar\Gamma_p$, $W_0 = P_0 g_2/2\Gamma_p\Gamma_r$, and $W_r = P_r g_2/2\Gamma_p\Gamma_r = f(r)\cos[\Delta l(\theta - \Omega t)]$ are the effective stationary and rotating potentials created by the pump with $f = \tilde{f}g_2/2\Gamma_p\Gamma_r$, and $\Omega$ is given in units of $2\Gamma_p$. $\alpha = g_1/g_2$ is the ratio of the gain and pump-induced blueshift, and $h = H\Gamma_r/4\hbar g_1\Gamma_p$ and $\tilde{h} = \tilde{H}\Gamma_r/4\hbar g_1\Gamma_p$ are normalized coefficients that account for the real and imaginary parts of the polariton nonlinearity.

## III. HYBRIDIZATION OF THE STATES IN ROTATING POTENTIALS

In this section, we consider the scenario in which the rotating potential couples the scalar states with angular indices $m = 0$ and $\pm 1$. This can be realized if an external nonresonant pump is created by the superposition of a simple Gaussian beam and a Laguerre-Gaussian beam with $l = \pm 1$. The shape of the rotating part of such a potential is schematically shown in Fig. 1(b).

The linearized equation (3) that describes the dynamics of the condensate close to the lasing threshold reads

$$i\partial_t\psi - \frac{1}{2}\nabla^2\psi + \left(V + \frac{i}{2}\right)\psi + (1 - i\alpha)W_0\psi = (i\alpha - 1)W_r\psi. \tag{4}$$

Let us assume the rotating potential is a small correction. This is a physically relevant case that allows us to develop a simple perturbation theory, giving a physical insight into the polariton dynamics.

The solution of the unperturbed equation (4) with the right-hand side set to zero can be expanded as

$$\psi = \sum_{m,q} C_{m,q}(t)\psi_{m,q}, \tag{5}$$

where $\psi_{m,q} = R_{m,q}(r)\exp im\theta$ are eigenfunctions of the azimuthally symmetric problem corresponding to the eigenvalues $\lambda_{m,q}$, with functions $R_{m,q}$ describing the radial condensate distribution, and $m$ and $q$ are angular and radial quantum numbers. For convenience, we use the normalized eigenfunctions, $\int|\psi_{m,q}|^2dxdy = 1$. The amplitude coefficients $C_{m,q}$ are governed by the equations

$$\dot{C}_{m,q} = \lambda_{m,q}C_{m,q}. \tag{6}$$

It is important to note that the eigenvalues $\lambda_{m,q}$ are, in general, complex, with the imaginary part representing the frequency of the eigenmode and the real part accounting for the effective losses caused by intrinsic dissipation and leakage of the mode through the potential barrier of finite width and height. In the presence of the pump, certain modes may formally exhibit negative effective losses (gain) and consequently grow exponentially in time. These modes are responsible for the polariton lasing in the considered geometry. As modes with higher radial quantum numbers $q$ are offset in energy and have substantially higher losses than the ground mode with $q = 0$, we neglect them in our further consideration and omit the index $q$ everywhere below.

Now we can consider the influence of the rotating potential as a small perturbation. Projecting Eq. (4) onto the unperturbed solutions of Eq. (6), we obtain the following equation for the amplitude coefficients $C_m$:

$$\dot{C}_m = \lambda_m C_m + (i + \alpha)(\eta_{m-}C_{m-\Delta l}e^{-i\Delta l\Omega t} + \eta_{m+}C_{m+\Delta l}e^{i\Delta l\Omega t}), \tag{7}$$

where $\eta_{m\pm} = 2\pi\int f(r)R_{m\pm\Delta l}R_m^* r dr$ are overlap integrals that provide the coupling coefficients of the mode $m$ to the modes $m \pm \Delta l$.

Let us consider the condition that needs to be satisfied for strong intermode coupling. The energies of the eigenmodes are schematically shown in Fig. 2, where the horizontal axis

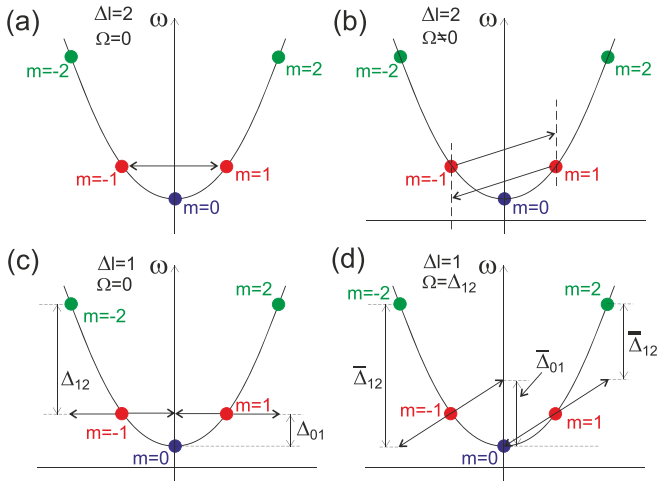


FIG. 2. Schematic representation of energy levels of linear modes of polaritons in a symmetric potential. The vertical axis represents the eigenenergies of the modes, and the horizontal axis denotes the quantized angular momentum $m$. Only the modes corresponding to the lowest radial quantum number are displayed. Panel (a) illustrates the coupling of the states with $m = \pm 1$ by a stationary potential with $\Delta l = 2$. Panel (b) demonstrates the detuning of states from resonance due to the suppression of hybridization of the $m = 1$ and $-1$ modes when the potential rotates. Panels (c) and (d) illustrate the hybridization of the $m = \pm 1$ states by stationary and rotating potentials with $\Delta l = 1$, respectively (see the text for more details).

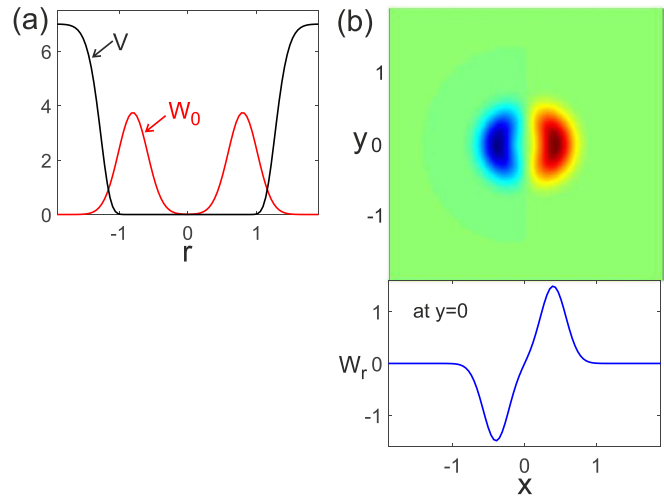


FIG. 3. (a) Potentials created by the microstructuring, $V$, and by the radially symmetric pump, $W_0$. (b) The spatial distribution of the rotating potential $W_r$. The upper part of the panel shows a 2D pattern of the potential, while the cross section of the potential $W_r$ by the $y = 0$ plane is shown in the lower part of the panel. In numerical simulations, the potential $V$ is defined as $V = V_0\{\exp[-(r - R_V)^8/w_V^8] + \exp[-(r + R_V)^8/w_V^8]\}$, with $V_0 = 7$, $R_V = 2.25$, and $w_V = 1$. The radially symmetric potential is $W_0 = \tilde{W}_0\{\exp[-(r - R_W)^2/w_W^2] + \exp[-(r + R_W)^2/w_W^2]\}$ with $\tilde{W}_0 = 3.75$, $R_W = 0.8$, and $w_W = 0.3$, and finally the rotating potential $W_r = \tilde{W}_r\{\exp[-(r - R_r)^2/w_r^2] - \exp[-(r + R_r)^2/w_r^2]\}\cos(\theta)$ with $\tilde{W}_r = 1.5$, $R_r = 0.4$, and $w_r = 0.25$. In this figure and all subsequent ones, spatial coordinates and parameters are scaled to the polariton propagation length $\sqrt{\hbar/2m^*\Gamma_p}$.

is the angular index of the mode and the vertical axis is the mode frequency. The condition of the strong coupling of the two modes requires that the angular indices of the modes, $m_1$ and $m_2$, differ by the angular index of the potential, $\Delta l$, and the frequencies of the interacting states, $\omega_{m1}$ and $\omega_{m2}$, differ by $\Omega\Delta l$. This can be formulated as a phase-matching condition:

$$m_1 = m_2 + \Delta l, \tag{8a}$$

$$\omega_{m1} = \omega_{m2} + \Omega\Delta l. \tag{8b}$$

Let us start with the case $\Delta l = 2$. One can easily see that for zero angular velocity, the stationary potential strongly couples the states with $m = \pm 1$, which are degenerate in energy; see Fig. 2(a). When the potential starts rotating, effective detuning in the rotation frame appears, which weakens the coupling, as illustrated in Fig. 2(b). It should be noted that, in general, a rapidly rotating potential can efficiently couple states such as $m = 1$ and 2 or $m = 1$ and 3. In these cases, the physics of the mixing is similar to that between $m = 0$ and $m = \pm 1$ states. However, this latter case requires slower rotation velocities to observe the discussed effects, which is advantageous from an experimental viewpoint. Thus, in this paper, we focus on the rotating potential with $\Delta l = 1$, which couples the states with $m = 0$ and $\pm 1$.

The stationary potential corresponding to $\Delta l = 1$ cannot efficiently couple the states because the states with $m_2 - m_1 = 1$ always have different eigenfrequencies [see Fig. 2(c), where it can be observed that the states with $m = \pm 1$ are detuned by some frequency $\Delta_{01}$ from the state with $m = 0$ and by $\Delta_{12}$ from the states with $m = \pm 2$]. However, rotation with velocity $\Omega = \Delta_{01}$ couples the state $m = 1$ to the state $m = 0$; see Fig. 2(d). It is worth mentioning that this rotation is not sufficient to couple the state $m = 1$ to the state $m = 2$ as nonzero detuning $\bar{\bar{\Delta}}_{12}$ is maintained. Note that this rotation couples the state $m = -1$ neither to the state $m = 0$ nor to the state $m = -2$ as the corresponding detunings in the rotating frame are increased to $\bar{\Delta}_{01}$ and $\bar{\Delta}_{12}$, respectively. This way, the symmetry $\theta \to -\theta$ gets broken: When the rotating potential is present, the state with angular momentum $m = 1$ undergoes hybridization with the state $m = 0$, while the state with angular index $m = -1$ remains almost unaffected by the rotating potential. Therefore, one can anticipate that the properties of the states $m = \pm 1$ change differently when subjected to a rotating potential.

## IV. NUMERICAL STUDIES OF POLARITONS IN ROTATING POTENTIALS WITH ANGULAR INDEX $\Delta l = 1$

To check our hypothesis, we performed numerical simulations using potentials shown in Fig. 3. The dimensionless parameter $\alpha$ defining the ratio of the gain to the polariton frequency shift created by the pump was set to 0.33. The dimensionless nonlinear coefficients accounting for the polariton interactions and nonlinear losses were chosen to be $h = 0.0186$ and $\tilde{h} = 0.001$, respectively. The corresponding values of dimensional parameters in Eq. (2) are given in [39].

It has been established [40] that by adjusting the parameters of a pump beam, it is possible to selectively excite the modes with well-defined angular and radial indices. For our simulation, we choose the potential $W_0$ such that, in the

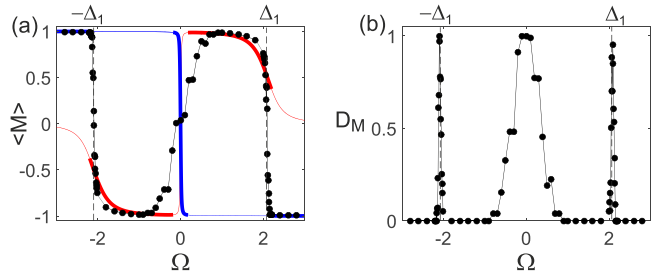


FIG. 4. (a) The normalized angular momenta of stationary polariton states obtained from 2D numerical simulations (black dots) and of the two fastest growing modes obtained using the perturbation theory (red and blue curves) as functions of the potential rotation velocity Ω. The thicker sections of the curves indicate the mode with the highest growth rate. In the 2D simulations, the angular momenta are averaged over the results of the series of $N = 100$ runs, each starting from random initial conditions, $\langle M\rangle = \frac{\sum_{j=1}^{N} M_j}{N}$, where $M_j$ is the normalized angular momentum in the $j$th run. (b) The dispersion $D_M = \frac{\sum_{j=1}^{N}(M_j-\langle M\rangle)^2}{\sum_{j=1}^{N} M_j^2}$ of the angular momenta obtained from 2D simulations; see the text for more details. The thin line connecting the circles is a guide for the eyes. Values of $\Omega = \pm\Delta_1$ at which the resonant mode coupling occurs are indicated by vertical dashed lines; see the text and Fig. 6 for details. In this figure and all subsequent ones, frequency parameters, including the rotation velocity of the potential Ω, are scaled to twice the polariton decay rate $2\Gamma_p$.

absence of the rotating pump, a condensate with the lowest radial index and angular momentum $\pm 1$ is created. Because of the symmetry, the modes with $m = +1$ and $-1$ are excited with equal probability. The potential also supports the fundamental mode, which exhibits slightly higher effective losses compared to the modes with $m = \pm 1$ (given the chosen set of parameters). The other modes have poor localization and high effective losses, which allows us safely to assume that they do not significantly impact the dynamics.

We performed a series of numerical simulations corresponding to different angular velocities of the rotating potential ($N = 100$ simulations for each frequency). We calculated the number of polaritons $E = \int |\psi|^2 d^2\mathbf{r}$ and the angular momentum

$$\mathcal{M} = i\int \psi^*(y\partial_x - x\partial_y)\psi d^2\mathbf{r} \tag{9}$$

of stationary polariton states in each round of the simulations. To characterize the rotation of the condensate, it is convenient to introduce its normalized angular momentum, defined as $M = \mathcal{M}/E$. The dependency of this quantity averaged over the number of realizations on the angular velocity of the potential is shown in Fig. 4(a) by solid circles. Panel (b) shows the dispersion of the angular momentum defined as

$$D_M = \frac{\sum_{j=1}^{N}(M_j - \langle M\rangle)^2}{\sum_{j=1}^{N} M_j^2}, \tag{10}$$

where $M_j$ is the normalized angular momentum calculated in the $j$th round of simulations, and $\langle M\rangle = (\sum_{j=1}^{N} M_j)/N$ is the normalized angular momentum averaged over $N$ simulations with different random initial conditions. It is seen that the dispersion deviates significantly from zero only in the vicinity of the potential angular velocities at which a change in the direction of polariton rotation occurs. A comprehensive explanation of this fact is provided in the subsequent section, where the perturbation theory is developed.

The distinction between the states formed at different rotation velocities is illustrated in Fig. 5, which displays the density and phase distribution of the stationary polariton states calculated at $\Omega = \pm 2.2$ and $\pm 1.9$. From this visualization, it can be deduced that polaritons generated in potentials rotating at velocities $\Omega = \pm 1.9$ and $\pm 2.2$ exhibit opposite rotation directions.

The results of the simulation clearly demonstrate that the normalized angular momentum of the stationary polaritons is an odd function of the angular velocity of the potential: $M(\Omega) = -M(-\Omega)$. However, a significant finding is that there exist specific nonzero potential rotation velocities at which both the sign and the absolute value of the polariton angular momentum undergo abrupt changes. Below, we show that these velocities act as thresholds that separate different ranges of potential angular velocities, where polaritons condense into distinct states. Importantly, these stationary states possess rotation velocities with different signs and absolute values. Figure 4 clearly illustrates this transition occurring at $\Omega \approx \pm 2$.

## V. PERTURBATION THEORY FOR POLARITONS IN ROTATING POTENTIALS WITH $\Delta l = 1$

To explain the observed phenomenon, we construct a simple coupled-mode theory based on Eq. (7). In our case, when $\Delta l = 1$, we take into account the interaction between the modes with $m = 0$ and $\pm 1$ only assuming that the coupling with other modes is negligible within the considered frequency range. First, we determine the parameters of the eigenmodes for the chosen stationary potentials $V$ and $W_0$ in the absence of the rotating potential $W_r = 0$. The analysis of the field evolution reveals the presence of a few localized modes in the spectrum, with only three modes exhibiting relatively high $Q$ factors: $m = \pm 1$ and 0. Additionally, the frequency separation between the modes with $m = 0$ and $\pm 1$ was found to be approximately 2 in the dimensionless units used by us, while the frequency difference between the other modes was considerably larger; see the Appendix for more details. These findings support our assumption that a three-mode approximation is sufficient to analyze the dynamics of the system.

Let us rewrite Eq. (7) in the three modes approximation:

$$\dot{C}_{-1} = (-\gamma_1 + i\omega_1)C_{-1} + (i+\alpha)\eta_{10}C_0 e^{i\Omega t}, \tag{11a}$$

$$\dot{C}_0 = (-\gamma_0 + i\omega_0)C_0 + (i+\alpha)(\eta_{10}C_1 e^{i\Omega t} + \eta_{10}C_{-1}e^{-i\Omega t}), \tag{11b}$$

$$\dot{C}_1 = (-\gamma_1 + i\omega_1)C_1 + (i+\alpha)\eta_{10}C_0 e^{-i\Omega t}, \tag{11c}$$

where $\gamma_1$ and $\gamma_0$ are the effective losses of the modes with the angular indices $m = \pm 1$ and 0, respectively, which take into account the radiative losses and the effect of the nonrotating pump, $\omega_1$ and $\omega_0$ are real eigenfrequencies of the modes, and $\eta_{10}$ is the interaction strength between the modes. These parameters were determined from 2D numerical modeling (see

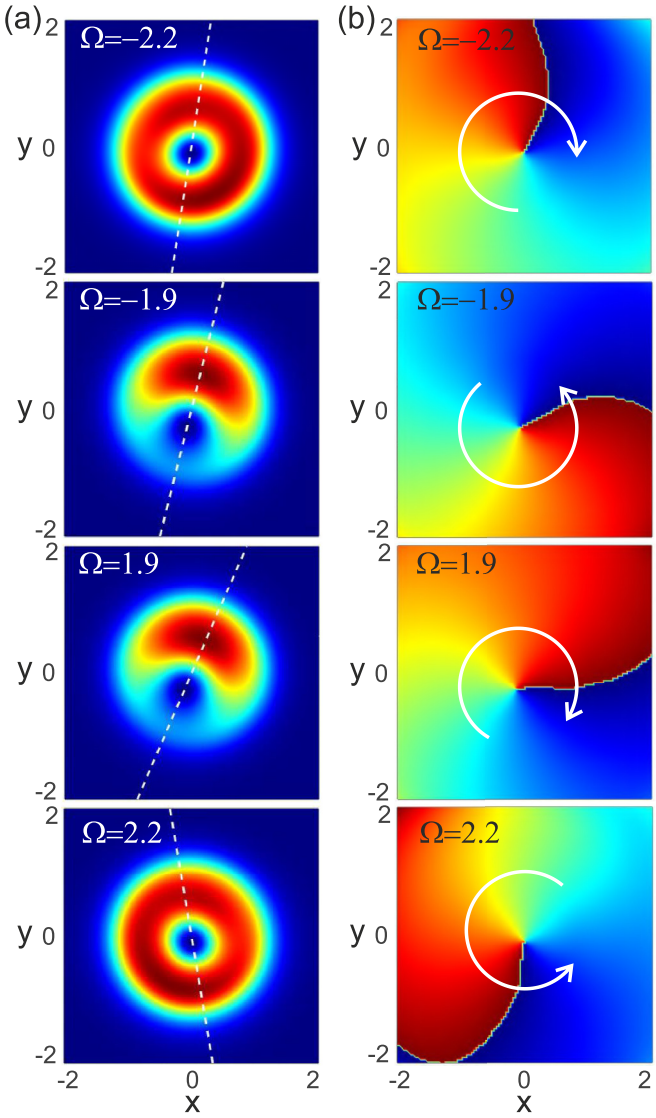


FIG. 5. The density (a) and phase (b) distributions for the stationary polariton states for the case of a potential corresponding to $\Delta l = 1$ rotating at angular velocities $\Omega = -2.2$, $-1.9$, 1.9, and 2.2. The thin blue dashed lines in panels (a) show the in-plane symmetry axis of the rotating potential. White round arrows in panel (b) indicate the direction of the rotation of the condensate. It is seen in (b) that the phase gradient is directed oppositely for the angular velocities of the potential equal to $\Omega = 1.9$ and 2.2 (the same is true for $\Omega = -1.9$ and $-2.2$). This means that polaritons can rotate in the same and in the opposite directions from the potential. It should also be mentioned that the polariton density distributions are quite different at $\Omega = 1.9$ and 2.2. At $\Omega = 1.9$, polaritons look like a pulse going round the trap, whereas at $\Omega = 2.2$ the polariton flux and density are distributed more or less evenly along the angular coordinate.

the Appendix for more details). It is worth noting that, for the determination of these constants, only a few simulations are necessary. Computationally, this approach is more efficient than solving the eigenvalue problem and subsequently calculating the corresponding overlap integrals. Additionally, it is worth mentioning that the coupled-mode approach not only speeds up simulations but also provides a pathway for

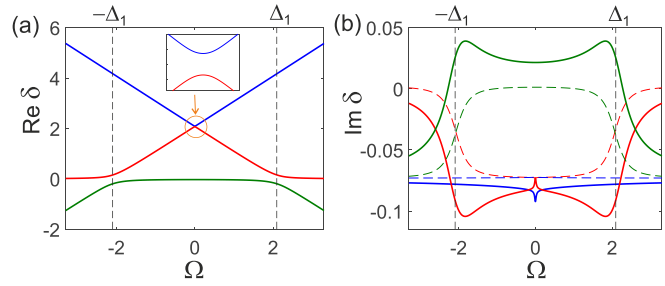


FIG. 6. The dependencies of the real (a) and imaginary (b) parts of the eigenfrequencies $\delta$ of the modes on the rotation velocity of the potential $\Omega$, calculated in the framework of the coupled mode theory. The dashed curves illustrate the case in which the rotating potential is pure conservative. Negative values of the imaginary part correspond to the modes growing in time. Values of $\Omega = \pm\Delta_1$ at which the resonant mode coupling occurs are indicated by vertical dashed lines.

analyzing the problem and investigating the mechanisms that govern the dynamics of polaritons.

We set the frequency $\omega_0$ of the mode with $m = 0$ as a reference frequency and express the other frequencies as detunings from $\omega_0$. We eliminate the explicit time dependence of the coupling coefficients by introducing new complex amplitudes,

$$A_1 = C_1 \exp^{-i(\omega_0+\Omega)t}, \tag{12a}$$

$$A_0 = C_0 \exp^{-i\omega_0 t}, \tag{12b}$$

$$A_{-1} = C_{-1} \exp^{-i(\omega_0-\Omega)t}. \tag{12c}$$

The equations for $A_{0,\pm1}$ can be written in the following form:

$$\dot{A}_{-1} = (-\gamma_1 + i\Delta_1 + i\Omega)A_{-1} + (i+\alpha)\eta_{10}A_0, \tag{13a}$$

$$\dot{A}_0 = -\gamma_0 A_0 + (i+\alpha)\eta_{10}(A_1 + A_{-1}), \tag{13b}$$

$$\dot{A}_1 = (-\gamma_1 + i\Delta_1 - i\Omega)A_1 + (i+\alpha)\eta_{10}A_0, \tag{13c}$$

where $\Delta_1 = \omega_1 - \omega_0$ is the detuning between the frequencies of the modes with $m = \pm1$ and $m = 0$.

Looking for the solution in the form $A \sim \exp(i\delta t)$, it is easy to find the eigenfrequencies $\delta$ and the eigenvectors $\vec{A} = (A_{-1}, A_0, A_1)^{\mathrm{T}}$ of the modes as functions of the angular velocity $\Omega$ of the potential. The dependencies of the real and imaginary parts of the eigenfrequencies $\delta$ are shown in Fig. 6 for the parameters corresponding to the 2D simulations discussed above. It should be noted that because of the pump, the values of $\gamma_{0,\pm1}$ can be negative, indicating that corresponding modes in the unperturbed problem (without the rotating potential) experience linear gain and thus grow in time.

As shown in Fig. 6(a), the real parts of the eigenfrequencies $\delta$ exhibit gaps at the rotation velocities $\Omega = 0$ and $\Omega = \pm\Delta_1$. The gap at $\Omega = 0$ arises from the interaction of the modes with $m = \pm1$ mediated by the mode with $m = 0$. Consequently, this gap is quadratic in $\eta_{10}$ and is thus small for shallow rotating potentials. The gaps at $\Omega = \pm\Delta_1$ occur due to the resonant scattering between the modes $m = 0$ and 1 caused by the rotating potential or, for the opposite sign of $\Omega$, between the modes with $m = 0$ and $-1$.

It is worth noting that in the vicinity of the resonant rotation velocity $\Omega \approx \pm\Delta_1$, the effect of the third mode can be

neglected, and the eigenfrequencies of two hybrid modes read

$$\delta_\pm = \tfrac{1}{2}\big[i(\gamma_0+\gamma_1)+\Delta_1+\Omega \pm i\sqrt{[\gamma_0-\gamma_1+i(\Delta_1+\Omega)]^2+4(1-i\alpha)^2\eta_{10}^2}\big] \quad (14)$$

for $\Omega \approx -\Delta_1$, and

$$\delta_\pm = \tfrac{1}{2}\big[i(\gamma_0+\gamma_1)+\Delta_1-\Omega \pm i\sqrt{[\gamma_0-\gamma_1+i(\Delta_1-\Omega)]^2+4(1-i\alpha)^2\eta_{10}^2}\big] \quad (15)$$

for $\Omega \approx \Delta_1$. Let us remark that the approximate analytical expression for the dependencies of $\delta(\Omega)$ can be obtained for the gap at $\Omega = 0$ as well.

It is important that the eigenfrequencies are complex, with their imaginary parts governing the growth (for $\mathrm{Im}\,\delta < 0$) or decay (for $\mathrm{Im}\,\delta > 0$) of a mode. As can be observed in Fig. 6(b), to the left of the resonance $\Omega = \Delta_1$, the red-colored mode is the fastest growing one, while the blue-colored mode is the second fastest growing. To the right of the resonance, the roles of the modes reverse, with the blue mode becoming the fastest growing.

Based on the linear mode analysis, we can propose the following scenario for the crossovers observed in our numerical simulations. If initial conditions are taken in the form of very low-intensity noise, the fastest growing mode eventually dominates and suppresses the growth of the other modes once it reaches the nonlinear regime. This scenario takes place when the lasing threshold is surpassed by only one mode.

When the pump intensity is close to the lasing threshold, nonlinear effects lead to the saturation of the mode but do not significantly alter its structure. In this case, one can anticipate that the structure of the stationary state closely resembles that of the fastest growing linear mode, and their normalized angular momenta coincide.

The dependencies of the normalized angular momenta $M$ of the fastest and the second fastest growing linear modes are shown in Fig. 4 in blue and red, respectively. The thicker lines indicate the range of $\Omega$ where a mode is the fastest growing. It is clearly seen that the angular momenta of the stationary states observed in the full-scale 2D simulations are very close to the angular momenta of the fastest growing linear mode.

Thus, our perturbation theory shows that if the pump is close to the lasing threshold, the stationary polariton state is determined by the fastest growing linear mode. Furthermore, the swap of the fastest and second fastest growing modes causes an abrupt change in the stationary polariton state. Now, let us delve into the reason behind the substantial deviation of the dispersion of the normalized angular momentum, as observed in a series of 2D simulations, in the vicinity of this transition; see Fig. 4.

The reason for this is that a mode with a smaller increment can win the competition if its initial amplitude is sufficiently higher than that of the fastest growing mode. To estimate the ratio of initial amplitudes at which the second fastest growing mode can prevail, we make a simple analysis. Let us assume that the nonlinear effects come into play, and the mode starts suppressing its competitors when its amplitude becomes equal to $a_{\mathrm{th}}$. We denote the increment and the initial amplitude of the fastest growing mode as $\gamma_f$ and $a_f$. Similarly, the increment and the amplitude of the second fastest growing mode are $\gamma_s$ and $a_s$. Let us find the condition providing that both modes reach the value $a_{\mathrm{th}}$ at the same time, $a_f \exp(\gamma_f t) = a_s \exp(\gamma_s t) = a_{\mathrm{th}}$. This time is given by $\ln(a_{\mathrm{th}}/a_f)$. The second fastest growing mode reaches the critical value earlier than the fastest mode if $a_s > a_f \exp(\frac{\gamma_f-\gamma_s}{\gamma_f}\ln\frac{a_{\mathrm{th}}}{a_f})$.

The latter formula reveals that the probability of the second fastest growing mode winning the competition depends on the intensity of the noise taken as the initial conditions. However, if the initial noise is weak, $a_f, a_s \ll a_{\mathrm{th}}$, the fastest and the second fastest growing modes have a comparable probability of winning only if the difference of the increments $\gamma_f - \gamma_s$ is small. This occurs at velocities close to the critical velocity at which the fastest and the second fastest modes swap, as at this point the increments are equal. This explains why the dispersion of the angular momentum in Fig. 4 is large in the vicinity of the resonant angular velocity $\Omega \approx 2$. In the regions of $\Omega$ where the difference in increments is large, the fastest growing mode always emerges as the winner.

It should be noted that this crossover does not occur in the case of purely conservative rotating potential. Indeed, for this case, there is no swap of the fastest and the second fastest growing modes, as can be seen in Fig. 5(b). Hence, one should expect a smooth dependency of the average angular momentum of polaritons on the rotation velocity of the potential, as shown by the blue line in Fig. 4.

Now, let us briefly discuss the behavior at small rotation velocities. In this case, there is another swap between the fastest and the second fastest growing modes for small angular velocities of the rotating potential around $\Omega \approx \pm 0.2$ for the chosen parameters. Consequently, there exists another threshold velocity $\Omega$ at which the normalized angular momentum of the condensate changes. However, the difference in growth rates between the competing modes is relatively small, and to observe the crossover, long simulation times are required, which renders full-scale 2D simulations costly.

For this reason, we performed numerical simulations of the coupled mode approximation generalized for the weakly nonlinear case. The dynamic equations for the modes can then be written as follows:

$$\dot{A}_{-1} = (-\gamma_1 + i\Delta_1 + i\Omega)A_{-1} + (i+\alpha)\eta_{10}A_0 + (\epsilon_{01}|A_0|^2 + \epsilon_{11}|A_{-1}|^2 + 2\epsilon_{11}|A_1|^2)A_{-1}, \quad (16a)$$

$$\dot{A}_0 = -\gamma_0 A_0 + (i+\alpha)\eta_{10}(A_1 + A_{-1}) + (\epsilon_0|A_0|^2 + \epsilon_{01}|A_1|^2 + \epsilon_{01}|A_{-1}|^2)A_0, \quad (16b)$$

$$\dot{A}_1 = (-\gamma_1 + i\Delta_1 - i\Omega)A_1 + (i+\alpha)\eta_{10}A_0 + (\epsilon_{01}|A_0|^2 + \epsilon_{11}|A_1|^2 + 2\epsilon_{11}|A_{-1}|^2)A_1, \quad (16c)$$

where $\epsilon_0$, $\epsilon_{ij}$ are complex constants defining the intramode ($\epsilon_0$, $\epsilon_{11}$) and intermode interactions ($\epsilon_{01}$) (see the Appendix for more details). The results are presented in Fig. 7.

The results obtained from the coupled-mode theory confirm the conclusion that the normalized angular momentum of polaritons near the lasing threshold is determined by the fastest growing linear mode. Figure 7(a) illustrates that the averaged angular momenta of the stationary polaritons closely align with the normalized angular momenta of the fastest

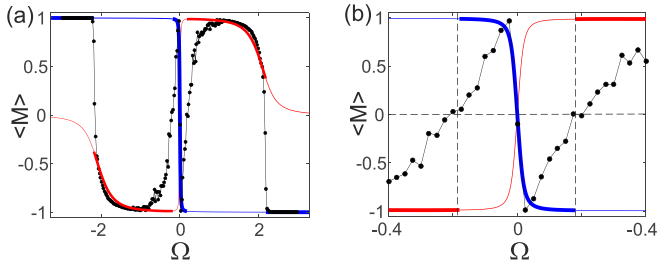


FIG. 7. (a) Normalized angular momenta of stationary states obtained from the coupled mode theory are shown by black filled circles (the thin black line connecting the circles is a guide for the eye). The red and blue lines show the normalized angular momenta of the two fastest growing modes as functions of the potential rotation velocity Ω. The thicker parts of the curves mark the fastest growing modes. (b) Same as in panel (a), but for a narrower frequency range. The vertical dashed lines mark the swap of the fastest and second fastest growing modes. The average normalized angular momentum changes it sign at $\Omega = 0$, $\Omega \approx \pm 0.2$ and $\Omega \approx \pm 2$.

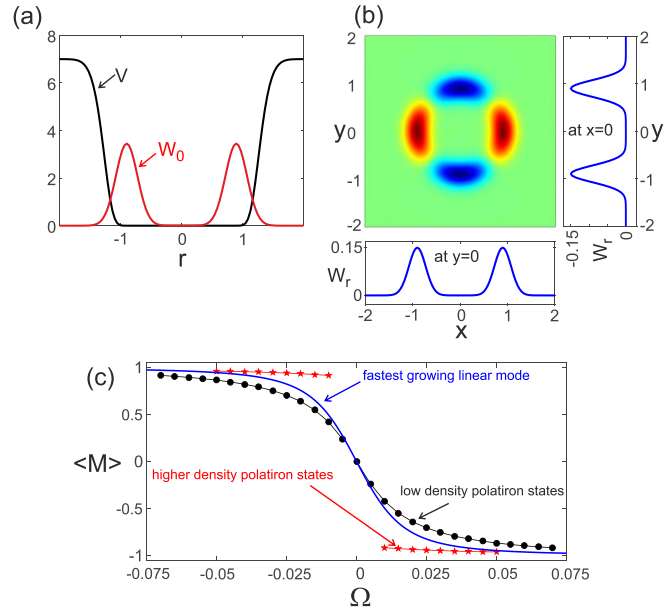


FIG. 8. (a) Potentials created by the microstructuring, $V$, and by the radially symmetric pump, $W_0$. (b) The spatial distribution of the rotating potential $W_r$. The 2D distribution of the potential is shown in the upper left part of the panel, while the cross sections of the potential $W_r$ by $y = 0$ and $x = 0$ planes are shown in the lower and upper right parts of the panel, respectively. The potential is created by the incoherent pump with an angular index difference $\Delta l = 2$. The parameters of the potentials $V$, $W_0$, and $W_r$ defined in the caption of Fig. 3 used for simulations are as follows: $V_0 = 7$, $R_V = 2.25$, and $w_V = 1$; $\tilde{W}_0 = 3.45$, $R_W = 0.9$, and $w_W = 0.25$; and $\tilde{W}_r = 0.15$, $R_r = 0.9$, and $w_r = 0.25$. (c) The averaged (over 100 simulations starting from a weak noise taken as the initial conditions) normalized polariton angular momentum as a function of the rotation velocity of the potential Ω for $\tilde{W}_0 = 3.45$ (solid black circles) and $\tilde{W}_0 = 3.75$ (red stars). One should note that at higher pump power, the polariton number $E$ in the stationary state is approximately five times larger than at the lower pump. The blue curve shows the dependency of the normalized angular momentum on Ω for the fastest growing linear mode calculated within the coupled mode approach for the parameters fitted to the full-scale 2D simulations.

growing linear mode, except in narrow ranges of the angular velocity Ω where the transitions between different polariton states occur.

Numerical simulations of coupled mode equations are much faster and allow for the collection of statistics through a large number of runs using very small random fields as initial conditions. This enables the accurate resolution of the transition occurring at $\Omega \approx 0.2$, as well as of the change of the polariton rotation at $\Omega = 0$. Figure 7(b) shows that the dependency of the normalized angular momentum of the stationary polaritons on Ω passes through zero at $\Omega = 0$ and at $\Omega \approx \pm 0.2$.

It should be noted that the smoothness of the transitions at $\Omega \approx 0.2$ is determined by the intensity of the initial noise used as the initial conditions. In an ideal scenario, these transitions should be sharp. However, achieving the desired sharpness is challenging due to the requirement of extremely low intensities for the initial conditions, necessitating very long numerical simulations. This is why, in our full-scale 2D simulations, we were unable to resolve these transitions completely but instead observed a large dispersion of the normalized angular momentum at the indicated angular velocities Ω, as shown in Fig. 4(b). This means that the difference between the increments of the fastest and the second fastest modes is so small that, for the chosen statistical properties of the initial conditions, these modes have comparable probabilities of winning.

At $\Omega = 0$, there is another change in the sign of the angular momentum of the condensate. This change is connected with the symmetry of the fastest growing mode. At $\Omega = 0$, the angular momentum of the fastest growing mode is exactly zero. However, the rotation of the potential breaks this symmetry, resulting in the appearance of the angular momentum of the stationary polariton state. Therefore, we can conclude that the changes in the sign of the angular momentum at $\Omega = 0$ and $\Omega \neq 0$ occur due to different physical reasons. At $\Omega \neq 0$, it is due to the swap between the two fastest growing modes, while at $\Omega = 0$, it is due to the change in symmetry of the fastest growing mode.

## VI. COMPARISON OF THE POLARITON DYNAMICS IN ROTATING POTENTIALS WITH $\Delta l = 1$ AND 2

The latter scenario discussed plays a key role in determining the angular momentum of polariton states in potentials that couple states with $m = \pm 1$ [37]. We performed numerical simulations using the potential shown in Fig. 8(a) with $\Delta l = 2$, which couples modes with $m = \pm 1$. The nonrotating axially symmetric potentials are shown in panel (b). The averaged normalized momenta of the stationary polariton states are shown in Fig. 8(c) for the excitation slightly above the polariton lasing threshold. It is clearly seen that the direction of the rotation of the potential determines the direction of the rotation of the condensate.

The density and the phase distributions of the stationary polariton states are shown in Figs. 9(a), 9(c) and 9(f) and Figs. 9(b), 9(d) and 9(e), respectively. The panels (a)–(d) correspond to the case of the pump slightly exceeding the lasing threshold. The direction of the condensate rotation is shown

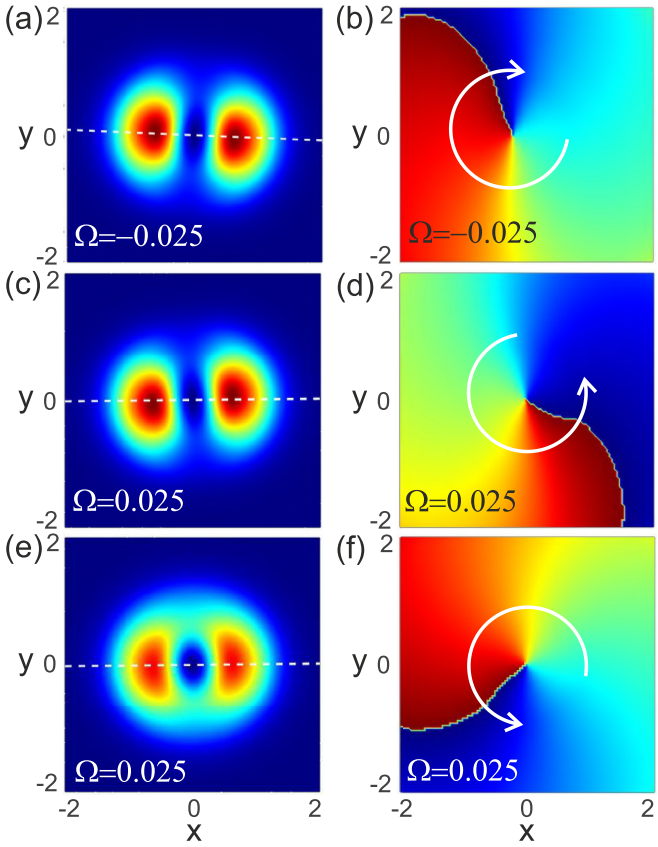


FIG. 9. Density (a),(c),(e) and phase (b),(d),(f) distributions corresponding to the stationary states for the case of the rotating potential with $\Delta l = 2$ and rotation velocities $\Omega = -0.025$ and 0.025. Thin white dashed lines in the left panels show the in-plane rotating potential symmetry axis passing through the potential maxima. Arrows in the right panels indicate the rotation direction of the polariton states. For (a)–(d), the stationary pump slightly exceeds the lasing threshold, $\tilde{W}_0 = 3.45$, whereas for (e),(f), the pump is more intense, $\tilde{W}_0 = 3.75$. The increase of the pump from $\tilde{W}_0 = 3.45$ to 3.75 results in the growth of the total polariton number $E$ in the stationary states by approximately five times. It is seen that for a higher incoherent pump, the variation of the polariton density along the angular coordinate becomes less pronounced.

by white arrows. Notably, the polariton density distribution consists of two lobes separated by dips. The separation becomes more pronounced at low rotation velocities; see panels (a),(c).

To establish the connection between the angular momentum of a stationary state and that of the corresponding fastest growing mode, we examined the coupled mode model [37]. In the case of a potential with $\Delta l = 2$, it is sufficient to take into account only two modes with $m = \pm 1$. By substituting

$$A_{\pm 1} = C_{\pm 1} e^{-i(\omega_1 \pm 2\Omega)t} \tag{17}$$

into (7), we get

$$\dot{A}_{\pm 1} = -(\gamma_1 \pm 2i\Omega)A_{\pm 1} + (i + \alpha)\eta_{\pm 1} A_{\mp 1}, \tag{18}$$

where $\eta_{\pm 1}$ is the coupling strength between the modes.

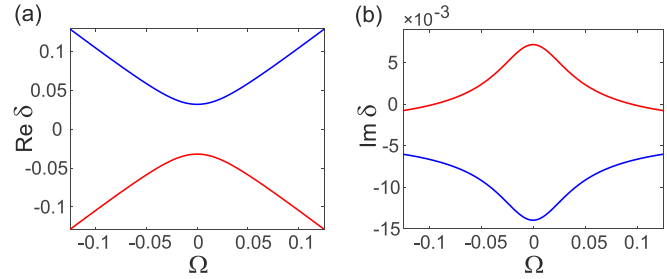


FIG. 10. The dependencies of the real (a) and imaginary (b) parts of the eigenfrequencies $\delta$ of the modes on the rotation velocity of the potential $\Omega$, calculated in the framework of the coupled mode theory. The negative values of the imaginary part correspond to a growing mode.

The eigenfrequencies $\delta_1$ of the modes can be easily found analytically, and they read

$$\delta_1 = i\gamma_1 \pm \sqrt{4\Omega^2 + (1 - i\alpha)^2 \eta_{\pm 1}^2}. \tag{19}$$

The eigenmodes have different linear growth rates due to the rotating spatially distributed linear gain. The dependencies of the real and imaginary parts of the eigenfrequencies $\delta_1$ on the rotation velocity $\Omega$ are depicted in Fig. 10. In this particular case, we observe that there is now a swap between the modes, and the same mode remains the fastest growing for all values of the angular velocity of the potential $\Omega$. Therefore, when $\Omega$ crosses zero, the change in the direction of polariton rotation occurs due to the corresponding change in the structure of the fastest growing mode. As a result, this change of the polariton velocity exhibits a smooth dependence on the potential rotation velocity $\Omega$. It is worth mentioning that, indeed, the normalized angular momentum of the stationary polariton state matches well with the normalized angular momentum of the fastest growing linear mode in the whole range of $\Omega$; see Fig. 8(c).

Thus, we can conclude that close to the lasing threshold, the formation of the stationary state is determined by the fastest growing mode, suppressing the other modes. Let us remark that when the initial conditions are taken as high-intensity noise, the resulting state becomes random, and we can observe, with different probabilities, the formation of the polariton states corresponding to different angular momenta.

Furthermore, it is important to note that at higher pump intensities, the impact of nonlinear effects on the structure of the growing field becomes significant. The normalized angular momentum as a function of the rotation velocity $\Omega$ obtained from the numerical simulations for a stronger pump is shown in Fig. 8(c) by the red stars. It is evident that the dependence deviates significantly from the one predicted by the linear mode analysis. It is also instructive to compare the density distributions of the stationary states formed at different pumps; see Figs. 9(d) and 9(e). It is seen that for relatively slow rotation velocities, a stationary state resembles a standing wave with deep minima. This standing wave is formed by counterpropagating waves with similar amplitudes and slightly different frequencies, causing the standing wave to rotate with the potential. A finite angular momentum of a polariton state arises due to the difference in the amplitudes

of the counterpropagating waves. At higher pumps, one of the waves becomes dominant, leading to an increase in the angular momentum of the state; see Fig. 8(c).

## VII. CONCLUSION

In conclusion, we developed a theory of the symmetry breaking in a polariton condensate formed in a stationary circular trap complemented with a weak rotating potential that helps hybridize the modes of the condensate with different quantized angular momenta. It is demonstrated that in the vicinity of the lasing threshold, a "winner takes all" scenario is realized, and the stationary state inherits the structure and normalized angular momentum of the fastest growing linear mode. We have also demonstrated that increasing the intensity of random initial noise can lead to the formation of stationary states different from the fastest growing states, with probabilities depending on the growth rates of these modes.

We have identified the critical speeds of rotation of the potential that induce the change of direction of the condensate rotation, and we identified two corresponding switching mechanisms. In the first case, the structure of the fastest growing mode changes in such a way that at some potential rotation velocity, the angular momentum of the mode changes its sign. In the second case, the fastest and second fastest growing modes swap at threshold velocity.

It is essential to acknowledge that the problem under consideration is closely connected to the formation of nonlinear vortices. However, the dynamics of vortices becomes significant only at relatively high polariton densities, given that the size of the vortex is smaller or comparable to the size of the trapping potential. In this paper, our focus is on excitations near the condensation threshold. Consequently, the polariton density is significantly lower than what is required for vortex formation.

## ACKNOWLEDGMENTS

I.A.S. acknowledges financial support from Icelandic Research Fund (Rannis, the project "Hybrid polaritonics"), "Priority 2030 Academic Leadership Program," and "Goszadanie no. 2019-1246." The numerical simulations performed by A.V.Y. were financially supported by the Russian Science Foundation (Project No. 23-72-00031). The work of E.S.S. was carried out within the state assignment in the field of scientific activity of the RF Ministry of Science and Higher Education (theme FZUN-2020-0013, state assignment of VlSU). A.V.K. and E.S.S. acknowledge Saint-Petersburg State University for the financial support (research Grant No. 94030557). A.V.K. acknowledges support of the Russian Foundation for Basic Research (Grant No. 19-52-12032).

## APPENDIX: DEVELOPMENT OF THE PERTURBATION THEORY FOR POLARITONS IN A ROTATING TRAP

Let us write Eq. (3) in the form

$$\partial_t \psi = i\hat{L}\psi + i\hat{P}\psi + iG(\psi), \tag{A1}$$

where $\hat{L} = -\frac{1}{2}\nabla^2 + (V + \frac{i}{2}) + (1 - i\alpha)W_0$ accounts for the linear properties of the systems in the absence of the rotating potential $W_r$. The terms associated with the rotating potential and the nonlinearity are $\hat{P} = (1 - i\alpha)W_r$ and $G(\psi) = (i\alpha - 1)(W_0 + W_r)\frac{|\psi|^2}{1+|\psi|^2}\psi + (h + i\tilde{h})|\psi|^2\psi$, respectively.

To proceed, we decompose the field into a series of eigenmodes of the unperturbed problem $\partial_t\psi = i\hat{L}\psi$. Because of the axial symmetry of the operator $\hat{L}$, the eigenmodes can be represented as $\psi_{m,q} = R_{m,q}(r)e^{im\theta}e^{i\omega_{m,q}t}$, where $\omega_{m,q}$ represent the corresponding eigenfrequencies of the operator $\hat{L}$: $\hat{L}\psi_{m,q} = \omega_{m,q}\psi_{m,q}$. The radial structure of the modes is described by the function $R_{m,q}$. The indices $q$ and $m$ are the radial and angular indices of the mode, respectively. In the further consideration, we use the fact that $R_{m,q} = R_{-m,q}$ for the operator $\hat{L}$. For the sake of convenience, we normalize the eigenfunctions as $\int |\psi_{m,q}|^2 dx\,dy = 1$. Let us acknowledge here that the eigenvalues $\omega_{m,q}$ are complex, accounting also for the linear losses (gain) experienced by the modes.

We look for a solution in the form (5) with coefficients $C_{m,q}(t)$ accounting for the temporal dynamics of the field. These coefficients evolve as $C_{m,q} = d_{m,q}e^{i\omega_{m,q}t}$, where $d_{m,q}$ are constants for the unperturbed problem. In the presence of perturbations, $d_{m,q}$ exhibits slow temporal dynamics. The validity of this approach relies on the condition that the perturbations are sufficiently weak, such that the characteristic evolution time $T_{\rm ch}$ of the mode amplitudes $d_{m,q}$ satisfies the condition $\min(|\omega_{m,q} - \omega_{m',q'}|T_{\rm ch}) \gg 1$.

We further impose the condition $|\psi| \ll 1$, which corresponds to low density of polaritons when they weakly deplete the reservoir of incoherent excitons. This condition is required to reduce the nonlinearity associated with the depletion of the pump to a cubic nonlinearity $(i\alpha - 1)W_0|\psi|^2\psi$, where, using the aforementioned assumptions, we have neglected the depletion of the rotating potential. Consequently, the nonlinear term can be expressed in the following form:

$$G(\psi) = U|\psi|^2\psi, \tag{A2}$$

where $U(r) = (h - W_0) + i(\tilde{h} + \alpha W_0)$ is the complex pseudopotential.

To develop the perturbation theory, we start with the linear intermode interactions induced by the rotating potential. By substituting (5) into (A1) and projecting onto the $\psi_{m,q}$ modes, we derive the equation for $d_{m,q}$ in the form

$$\dot{C}_{m,q} = i\omega_{m,q}C_{m,q} + \sum_{m',q'} C_{m',q'}\int \psi_{m',q'}\psi^*_{m,q}W_r dx\,dy. \tag{A3}$$

We consider the rotating potential of the form $W_r = (i + \alpha)f(r)\cos[\Delta l(\theta - \Omega t)]$, where $f(r)$ describes the radial dependency of the potential. Let us recall that $\Delta l$ is the number of maxima of the potential along the angular coordinate, and $\Omega$ is the potential rotation velocity. We make the derivation for the case of $\Delta l = 1$, which can be easily generalized to arbitrary $\Delta l$. Subsequently, the integrals can be calculated as

$$\int \psi_{m',q'}\psi^*_{m,q}W_r dx\,dy = \frac{1}{2}\int rR^*_{m,q}R_{m',q'}f(r)dr \times \int e^{i(m'-m+1)\theta - i\Omega t} + e^{i(m'-m-1)\theta + i\Omega t}d\theta.$$

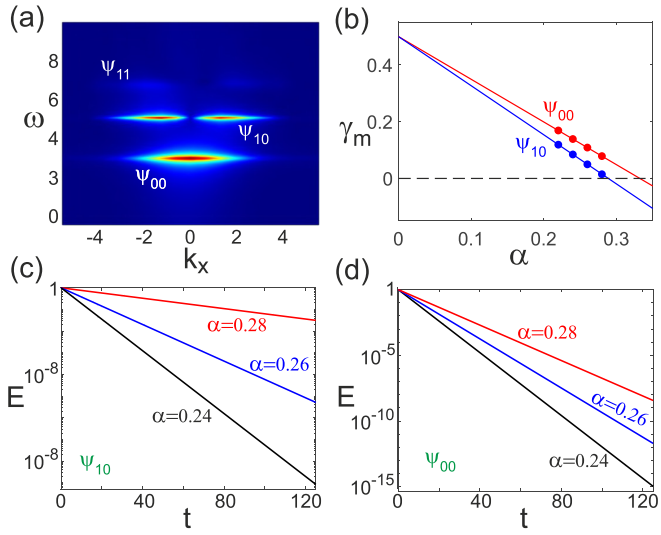


FIG. 11. (a) Cross section of the Fourier representation $\psi(k_x, k_y = 0, \omega)$ of the field $\psi(x, y, t)$. The patterns identified as the modes with $m = 0$ and $q = 0$, $m = 1$ and $q = 0$, and $m = 1$ and $q = 1$ are marked as $\psi_{00}$, $\psi_{10}$, and $\psi_{11}$, respectively. (b) The dependencies of the decay rates of the modes $\psi_{00}$ and $\psi_{10}$ as functions of $\alpha$. The solid circles are the calculated points, while the thin lines are a guide for eye. The dashed line marks the zero of the decay rates. (c),(d) The temporal dependencies of the occupancy of the modes $\psi_{01}$ and $\psi_{00}$ on time for different values of $\alpha$. The time axis is chosen such that at $t = 0$, only the one mode from the initial field distributions survives. For convenience, the occupancies $E$ are scaled such that at $t = 0$ they are all equal to unity. Please see the text for more details. In this figure and all subsequent ones, time is scaled to the inverse of twice the polariton decay rate $1/2\Gamma_p$.

This term is nonzero only for $m' = m - 1$ and $m' = m + 1$. Then the equations for $C_{m,q}$ can be reduced to

$$\dot{C}_{m,q} = i\omega_{m,q}C_{m,q} + (i+\alpha)\sum_{q'}\sigma_{m,+,q,q'}e^{i\Omega t}C_{m+1,q'} + \sigma_{m,-,q,q'}e^{-i\Omega t}C_{m-1,q'}, \tag{A4}$$

where $\sigma_{m,\pm,q,q'} = \pi\int rR^*_{m,q}R_{m\pm1,q'}f(r)dr$.

Typically, only a few modes exhibit negative or low positive losses, which aligns well with the results presented in the main part of the paper. To obtain the coefficients required for the perturbation theory, we conducted several numerical experiments. Initially, let us determine the eigenfrequencies of the polariton modes, specifically for the case of small $\alpha$, where the gain does not significantly impact the mode structure. Under this condition, the real parts of the eigenfrequencies remain independent of $\alpha$. Therefore, we choose $\alpha = 0.26$, slightly below the smallest lasing threshold, and perform the simulation starting with the initial conditions in the form of $\psi = a\sum_{m=0}^{4} e^{-r^2/r_0^2}e^{im\theta}$, where $a = 0.001$ is the small amplitude and $r_0 = 1$ is the radius of the initial field distribution. The rotating potential is set to zero.

The results of the numerical simulations are presented in Fig. 11(a) displaying the Fourier representation $\psi(k_x, k_y, \omega)$ of the field $\psi(x, y, t)$. In this panel, one can easily identify the pattern corresponding to the mode with $m = 0$, $q = 0$ marked as $\psi_{00}$. At the higher frequency, there is a pattern corresponding to the mode $\psi_{10}$ with $m = 1$, $q = 0$. By calculating the positions of the spectral lines, we determine the eigenfrequencies of the modes.

It is worth noting that for the chosen parameters, the width of the spectral line of the mode $\psi_{10}$ is smaller compared to that of the mode $\psi_{00}$, indicating a higher quality factor for the modes $\psi_{\pm10}$. Additionally, a faint pattern corresponding to the mode $\psi_{11}$ is observed at an even higher frequency, but its quality factor is significantly lower. Let us remark that the eigenfrequency of this mode is close to the maximum height of the confining potential, suggesting that radiative losses are expected to be very high for this mode and for the modes with higher frequencies.

By conducting numerical simulations and monitoring the decay of the polariton number $E = \int|\psi|^2dx\,dy$ over time, it is straightforward to determine the mode decrements as functions of the parameter $\alpha$. By choosing appropriate symmetry of the initial conditions, it is possible to distinguish the modes with different $m$. Thus, the initial distribution contains modes with fixed $m$ but different $q$. However, the modes with different $q$ have different decay rates, and eventually only the mode with the slowest decay rate survives. This way, we estimate the mode decrements as functions of $\alpha$ for the modes $\psi_{10}$ and $\psi_{00}$; see Fig. 11(b). To demonstrate that we conduct estimation at times when the field contains only one mode, we plotted the dependencies of the polariton number $E$ on time; see Figs. 11(c) and 11(d). One can see that these dependencies exhibit linear behavior on the logarithmic scale.

As expected for a weakly dissipative system, the decay rates of the modes depend linearly on the parameter $\alpha$, which represents the ratio of the imaginary part of the potential to its real part. It is possible to extrapolate the dependencies for finding the effective losses for the parameter $\alpha = 0.33$ used in the numerical simulations. It should be noted that the mode decrements become negative at some threshold $\alpha$, indicating mode growth. This method also provides the ability to identify the mode with the longest lifetime among the modes with a fixed angular index $m$.

Finding the modes with the second smallest decay rate is more challenging. However, an estimation of their decay rate can be obtained by examining the beating between the modes. The decay rate of this beating provides the difference between the decay rates of the modes with the first and second smallest decay rates. By conducting this estimation, we discovered that the decay rate of the mode $\psi_{11}$ is more than an order of magnitude higher than the decay rate of the mode $\psi_{10}$. This observation supports the assumption that, in the first approximation, the dynamics of the system can be described in terms of the amplitudes of the modes $\psi_{00}$ and $\psi_{\pm10}$.

Thus, we disregard all modes except the three modes with $m = \pm1$, $m = 0$, and $q = 0$. Subsequently, the equations for the coefficients $d_{\pm1}$, $d_0$ take the following form:

$$\dot{C}_{-1} = i\omega_1C_{-1} + \eta e^{i\Omega t}C_0, \tag{A5a}$$

$$\dot{C}_0 = i\omega_0C_0 + \eta(e^{-i\Omega t}C_{-1} + e^{i\Omega t}C_1), \tag{A5b}$$

$$\dot{C}_1 = i\omega_1C_1 + \eta e^{-i\Omega t}C_0. \tag{A5c}$$

Here and everywhere below, we omitted the second index, $q$, for it is always zero. We also used the equalities $\omega_m = \omega_{-m}$ and $R_m = R_{-m}$ that follow from the degeneracy of the modes

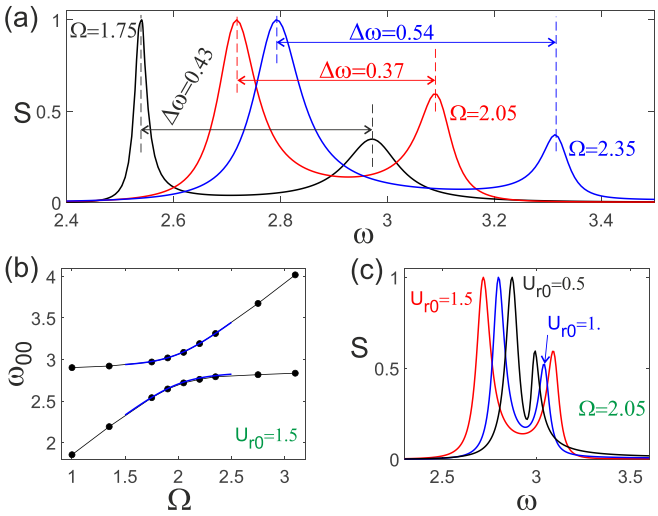


FIG. 12. (a) The temporal spectra of the field for different potential rotation velocities of the potential Ω. The frequency differences $\Delta\omega$ between the peaks are given in the panel. (b) The positions of the spectral peaks in the vicinity of the eigenfrequency of $\psi_{00}$ state as functions of Ω. The black solid circles are the data extracted from 2D simulations, and the blue curves are the fit by formula (14). The thick black lines are a guide for the eye. (c) The spectra calculated for the different amplitudes of the potential rotating at the velocity $\Omega = 2$.

with angular indices $\pm m$. This is why $\sigma_{-1,+} = \sigma_{0,-} = \sigma_{0,+} = \sigma_{1,-}$, and we denote this as $\eta_{10}$.

To use the coupled mode approach, it is necessary to determine the values of the scattering rates $\eta_{10}$. These values can be found from 2D numerical simulations. We choose $\alpha$ slightly below the lasing threshold for $\psi_{10}$ mode and take the initial distribution in the form $\psi = ae^{-r^2/w^2}e^{i\theta}$. Then we conduct numerical simulations in the presence of the conservative rotating potential and calculate the temporal spectra of the field.

The presence of the rotating potential with $\Delta l = 1$ causes the coupling of the mode with $m = 1$ to the mode with $m = 0$. This process is most effective when the rotation velocity Ω matches the frequency difference between the modes $\psi_{00}$ and $\psi_{10}$. Indeed, when the frequency is close to 2, we observe the emergence of two spectral peaks with frequencies close to the eigenfrequency of the $\psi_{00}$ mode; see Fig. 12(a).

These peaks correspond to two hybrid modes formed by the mixing of $\psi_{10}$ and $\psi_{00}$ states. It is worth noting that each of the hybrid modes has two spectral lines, one near the frequency of the pure $\psi_{10}$ state and the other near the frequency of the $\psi_{00}$ state. For technical reasons, it is easier to estimate the spectral lines at frequencies close to the eigenfrequency of $\psi_{00}$ state.

The positions and the separation between the spectral lines of the hybrid modes are dependent on the rotation velocity of the potential; see Figs. 12(a) and 12(b). To confirm that the two peaks are indeed associated with the splitting caused by the rotating potential, we calculated the spectra for different amplitudes of the rotating potential. The results depicted in Fig. 12(c) show that, indeed, the frequency difference between the peaks decreases with the decrease of the rotating potential amplitude.

In the vicinity of the resonance frequency, this dependency can be approximated by (14). To estimate the scattering rate, we can disregard losses and fit the numerical data by the analytical expression (14) choosing the appropriate $\eta$. The fit, shown by the thicker blue line in Fig. 12(b), demonstrates good agreement between the analytical and numerical results.

Let us now turn to the perturbation induced by the nonlinear term. Looking for the solution in the form

$$\psi = C_{-1}R_1e^{-i\theta} + C_0R_0 + C_1R_1e^{i\theta},$$

we can calculate the nonlinear term and project it onto the eigenfunctions $\psi_{\pm1}$ and $\psi_0$. The projections $Y_{\pm1}$, $Y_0$ on the modes $m = -1$, 0, and 1 are given by the following expressions:

$$Y_{-1} = (\epsilon_{11}|C_{-1}|^2 + 2\epsilon_{11}|C_1|^2 + \epsilon_{01}|C_0|^2)C_{-1} + \tilde{\epsilon}_{01}C_0^2C_1^*, \tag{A6a}$$

$$Y_0 = (\epsilon_0|C_0|^2 + 2\epsilon_{01}|C_{-1}|^2 + \epsilon_{01}|C_1|^2)C_0 + \tilde{\epsilon}_{01}^*(C_0 + C_0^*)C_{-1}C_1, \tag{A6b}$$

$$Y_1 = (\epsilon_{11}|C_1|^2 + 2\epsilon_{11}|C_{-1}|^2 + \epsilon_{01}|C_0|^2)C_1 + \tilde{\epsilon}_{01}C_0^2C_{-1}^*, \tag{A6c}$$

where the nonlinear interaction constants are $\epsilon_{11} = 2\pi\int Ur|R_1|^4dr$, $\epsilon_{01} = 4\pi\int Ur|R_0|^2|R_1|^2dr$, $\epsilon_0 = 2\pi\int Ur|R_0|^4dr$, and $\tilde{\epsilon}_{01} = 2\pi\int UrR_0^2R_1^{*2}dr$.

It is worth noting that the first term in (A6a) has a frequency close to the frequency of the mode $\omega_1$ provided that, according to the derivation, the mode amplitudes $C$ can be represented as $C_m = d_me^{i\omega_m t}$, where $d_m$ is a slowly varying function of time. However, the frequency of the second term can be estimated as $2\omega_0 - \omega_1$. This would cause the dynamics of the mode amplitude $d_{-1}$ at the frequency $2|\omega_0 - \omega_1|$, which is, obviously, not small compared to the detuning of the mode eigenfrequencies. Therefore, this term cannot be included in the equation for $C_1$ but, if necessary, can be taken into account through an additional small correction to the field. Similarly, it can be observed that the last terms in the expressions for $Y_0$ and $Y_1$ do not contribute to the equations for the amplitudes $C_0$ and $C_1$. Thus, accounting for the nonlinear interaction, the equations for the mode amplitudes can be written as follows:

$$\dot{C}_{-1} = i\omega_1C_{-1} + (i+\alpha)\eta_{10}e^{i\Omega t}C_0 + (\epsilon_{11}|C_{-1}|^2 + 2\epsilon_{11}|C_1|^2 + \epsilon_{01}|C_0|^2)C_{-1}, \tag{A7a}$$

$$\dot{C}_0 = i\omega_0C_0 + (i+\alpha)\eta_{10}(e^{-i\Omega t}C_{-1} + e^{i\Omega t}C_1) + (\epsilon_0|C_0|^2 + \epsilon_{01}|C_{-1}|^2 + \epsilon_{01}|C_1|^2)C_0, \tag{A7b}$$

$$\dot{C}_1 = i\omega_1C_1 + (i+\alpha)\eta_{10}e^{-i\Omega t}C_0 + (\epsilon_{11}|C_1|^2 + 2\epsilon_{11}|C_{-1}|^2 + \epsilon_{01}|C_0|^2)C_1. \tag{A7c}$$

Now changing the variables $A_1 = C_1\exp^{-i(\omega_{0r}+\Omega)t}$, $A_0 = C_0\exp^{-i\omega_{0r}t}$, and $A_{-1} = C_{-1}\exp^{-i(\omega_{0r}-\Omega)t}$, where $\omega_{0r} = \mathrm{Re}\,\omega_0$, we arrive at the equations for the amplitudes $A$:

$$\dot{A}_{-1} = (-\gamma_1 + i\Delta_1 + i\Omega)A_{-1} + (i+\alpha)\eta_{10}A_0 + (\epsilon_{11}|A_{-1}|^2 + 2\epsilon_{11}|A_1|^2 + \epsilon_{01}|A_0|^2)A_{-1}, \tag{A8a}$$

$$\dot{A}_0 = -\gamma_0A_0 + (i+\alpha)\eta_{10}(A_1 + A_{-1}) + (\epsilon_0|A_0|^2 + \epsilon_{01}|A_{-1}|^2 + \epsilon_{01}|A_1|^2)A_0, \tag{A8b}$$

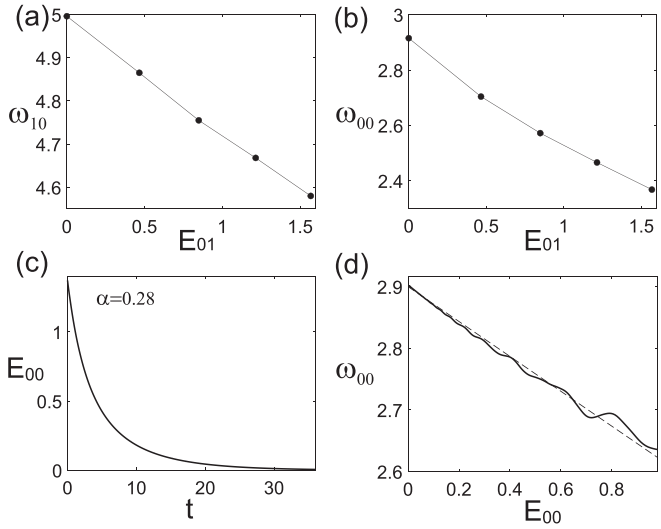


FIG. 13. (a) The dependency of the frequency $\omega_{10}$ of the stationary state $\psi_{10}$ on its polariton number $E_{10}$. (b) The frequency of the weak perturbation having the structure of the state $\psi_{00}$ nestling on the stationary state $\psi_{10}$ as a function of the total number of polaritons $E_{10}$ in the state $\psi_{10}$. (c) The temporal evolution of the polariton number $E_{00}$ of the state $\psi_{00}$ for the parameter $\alpha$ below the lasing threshold. (d) The instantaneous frequency $\omega_{00} = \frac{\partial_t Q}{Q}$ of the decaying state $\psi_{00}$ as a function of the total number of polaritons $E_{00}$ in the state $\psi_{00}$. The parameter $Q$ is defined as $Q = \int \psi \, dx \, dy$. The thinner dashed line in this panel is the linear fit for the numerically calculated curve.

$$\dot{A}_1 = (-\gamma_1 + i\Delta_1 - i\Omega)A_1 + (i+\alpha)\eta_{10}A_0 + (\epsilon_{11}|A_1|^2 + 2\epsilon_{11}|A_{-1}|^2 + \epsilon_{01}|A_0|^2)A_1, \quad \text{(A8c)}$$

where $\gamma_1 = \mathrm{Im}\,\omega_1$, $\gamma_0 = \mathrm{Im}\,\omega_0$, and $\Delta_1 = \mathrm{Re}\,\omega_1 - \omega_{0r}$.

Next, we need to determine the values of the nonlinear interaction constants. We start by estimating the imaginary parts of $\epsilon$'s. For this purpose, we perform numerical simulations of the problem without the rotating potential while maintaining $\alpha$ above the lasing threshold for the mode $\psi_{10}$ but below the lasing threshold of the mode $\psi_{00}$. As a result, only the state $\psi_{10}$ can form in the system. The frequency of the stationary state can be found from the position of the maximum of its temporal spectrum. The polariton number of the stationary state $E_{10}$ can be controlled by changing the value of $\alpha$. This way it is possible to find the dependency of the frequency of the stationary state on its polariton number. This dependency is shown in Fig. 13(a). It is seen that the dependency is quite linear, which proves that the nonlinearity can be accurately approximated by a cubic nonlinearity. The slope of the line gives the value of the coefficient $\mathrm{Im}\,\epsilon_{11}$.

To find the coefficient $\mathrm{Im}\,\epsilon_{01}$, we perturb the stationary state $\psi_{11}$ by the state $\psi_{00}$ of very low intensity. Then we measure the frequency of the state $\psi_{00}$ which depends on the polariton number of the state $\psi_{10}$. The frequencies of the states $\psi_{00}$ and $\psi_{10}$ are well resolved, so the frequency of the state $\psi_{00}$ can be measured easily. The dependency of the frequency $\omega_{00}$ of the small perturbation $\psi_{00}$ on the polariton number $E_{10}$ of the stationary nonlinear state $\psi_{10}$ is shown in Fig. 13(b). As is expected, the dependency is close to 1 in the linear case as well.

To determine the coefficient $\epsilon_{00}$ characterizing the nonlinear self-action of the mode $\psi_{00}$, we take the initial conditions in the form of the field with the angular index $m = 0$ with rather high intensity. To avoid the excitation of the state $\psi_{10}$, we set $\alpha$ below the lasing threshold. In these circumstances, the polariton number of the state $\psi_{00}$ decays quasiexponentially; see Fig. 13(c). The change in intensity of the state leads to variations in its frequency and decrement. The instantaneous frequency can be obtained by calculating the function $\frac{\partial_t Q}{Q}$, where $Q = \int \psi \, dx \, dy$. The dependency of the frequency $\omega_{00}$ on the polariton number $E_{00}$ of the mode $\psi_{00}$ is shown in Fig. 13(d). The dependency is also close to 1 in the linear case. The deviation can be explained by the contribution of the modes with higher radial indices. The slope of the dependency allows us to determine $\mathrm{Im}\,\epsilon_{00}$.

Let us note that by measuring the decay rates of the modes, one can obtain the values of the real part of $\epsilon$, which quantify the strength of the nonlinear losses. For the chosen parameters, the real parts of $\epsilon$ can be approximated by the formula $\mathrm{Re}\,\epsilon = \alpha\,\mathrm{Im}\,\epsilon$, since the dominant nonlinearity arises from pump depletion. Furthermore, it is worth mentioning that the same approach described above can be used to determine the parameters for the coupled mode approximation in the case of a potential with $\Delta l = 2$.


[1] I. Carusotto and C. Ciuti, Quantum fluids of light, Rev. Mod. Phys. **85**, 299 (2013).

[2] J. Kasprzak, M. Richard, S. Kundermann, A. Baas, P. Jeambrun, J. M. J. Keeling, F. Marchetti, M. Szymańska, R. André, J. Staehli *et al.*, Bose–Einstein condensation of exciton polaritons, Nature (London) **443**, 409 (2006).

[3] R. Balili, V. Hartwell, D. Snoke, L. Pfeiffer, and K. West, Bose-Einstein condensation of microcavity polaritons in a trap, Science **316**, 1007 (2007).

[4] S. Pau, H. Cao, J. Jacobson, G. Björk, Y. Yamamoto, and A. Imamoğlu, Observation of a laserlike transition in a microcavity exciton polariton system, Phys. Rev. A **54**, R1789 (1996).

[5] S. Christopoulos, G. B. H. Von Högersthal, A. J. D. Grundy, P. G. Lagoudakis, A. V. Kavokin, J. J. Baumberg, G. Christmann, R. Butté, E. Feltin, J.-F. Carlin *et al.*, Room-temperature polariton lasing in semiconductor microcavities, Phys. Rev. Lett. **98**, 126405 (2007).

[6] C. Schneider, A. Rahimi-Iman, N. Y. Kim, J. Fischer, I. G. Savenko, M. Amthor, M. Lermer, A. Wolf, L. Worschech, V. D. Kulakovskii *et al.*, An electrically pumped polariton laser, Nature (London) **497**, 348 (2013).

[7] A. Kavokin, G. Malpuech, and F. P. Laussy, Polariton laser and polariton superfluidity in microcavities, Phys. Lett. A **306**, 187 (2003).

[8] I. Carusotto and C. Ciuti, Probing microcavity polariton superfluidity through resonant Rayleigh scattering, Phys. Rev. Lett. **93**, 166401 (2004).

[9] P. Cristofolini, A. Dreismann, G. Christmann, G. Franchetti, N. G. Berloff, P. Tsotsis, Z. Hatzopoulos, P. G. Savvidis, and J. J. Baumberg, Optical superfluid phase transitions and

trapping of polariton condensates, Phys. Rev. Lett. **110**, 186403 (2013).
[10] I. Yu. Chestnov, A. V. Yulin, A. P. Alodjants, and O. A. Egorov, Nonlinear bloch waves and current states of exciton-polariton condensates, Phys. Rev. B **94**, 094306 (2016).
[11] G. Lerario, A. Fieramosca, F. Barachati, D. Ballarini, K. S. Daskalakis, L. Dominici, M. De Giorgi, S. A. Maier, G. Gigli, S. Kéna-Cohen *et al.*, Room-temperature superfluidity in a polariton condensate, Nat. Phys. **13**, 837 (2017).
[12] V. A. Lukoshkin, V. K. Kalevich, M. M. Afanasiev, K. V. Kavokin, Z. Hatzopoulos, P. G. Savvidis, E. S. Sedov, and A. V. Kavokin, Persistent circular currents of exciton-polaritons in cylindrical pillar microcavities, Phys. Rev. B **97**, 195149 (2018).
[13] E. S. Sedov, V. A. Lukoshkin, V. K. Kalevich, P. G. Savvidis, and A. V. Kavokin, Circular polariton currents with integer and fractional orbital angular momenta, Phys. Rev. Res. **3**, 013072 (2021).
[14] E. Sedov, S. Arakelian, and A. Kavokin, Spontaneous symmetry breaking in persistent currents of spinor polaritons, Sci. Rep. **11**, 22382 (2021).
[15] V. Lukoshkin, E. Sedov, V. Kalevich, Z. Hatzopoulos, P. G. Savvidis, and A. Kavokin, Steady state oscillations of circular currents in concentric polariton condensates, Sci. Rep. **13**, 4607 (2023).
[16] D. Sanvitto, F. Marchetti, M. Szymańska, G. Tosi, M. Baudisch, F. P. Laussy, D. Krizhanovskii, M. Skolnick, L. Marrucci, A. Lemaitre *et al.*, Persistent currents and quantized vortices in a polariton superfluid, Nat. Phys. **6**, 527 (2010).
[17] K. G. Lagoudakis, M. Wouters, M. Richard, A. Baas, I. Carusotto, R. André, L. S. Dang, and B. Deveaud-Pledran, Quantized vortices in an exciton–polariton condensate, Nat. Phys. **4**, 706 (2008).
[18] K. Lagoudakis, T. Ostatnický, A. Kavokin, Y. G. Rubo, R. André, and B. Deveaud-Pledran, Observation of half-quantum vortices in an exciton-polariton condensate, Science **326**, 974 (2009).
[19] G. Nardin, G. Grosso, Y. Léger, B. Pietka, F. Morier-Genoud, and B. Deveaud-Pledran, Hydrodynamic nucleation of quantized vortex pairs in a polariton quantum fluid, Nat. Phys. **7**, 635 (2011).
[20] K. G. Lagoudakis, F. Manni, B. Pietka, M. Wouters, T. C. H. Liew, V. Savona, A. V. Kavokin, R. André, and B. Deveaud-Pledran, Probing the dynamics of spontaneous quantum vortices in polariton superfluids, Phys. Rev. Lett. **106**, 115301 (2011).
[21] Y. Xue, I. Chestnov, E. Sedov, E. Kiktenko, A. K. Fedorov, S. Schumacher, X. Ma, and A. Kavokin, Split-ring polariton condensates as macroscopic two-level quantum systems, Phys. Rev. Res. **3**, 013099 (2021).
[22] A. Kavokin, T. C. H. Liew, C. Schneider, P. G. Lagoudakis, S. Klembt, and S. Hoefling, Polariton condensates for classical and quantum computing, Nat. Rev. Phys. **4**, 435 (2022).
[23] M. Aßmann, F. Veit, M. Bayer, A. Löffler, S. Höfling, M. Kamp, and A. Forchel, All-optical control of quantized momenta on a polariton staircase, Phys. Rev. B **85**, 155320 (2012).
[24] R. Dall, M. D. Fraser, A. S. Desyatnikov, G. Li, S. Brodbeck, M. Kamp, C. Schneider, S. Höfling, and E. A. Ostrovskaya, Creation of orbital angular momentum states with chiral polaritonic lenses, Phys. Rev. Lett. **113**, 200404 (2014).
[25] G. Nardin, K. G. Lagoudakis, B. Pietka, F. Morier-Genoud, Y. Léger, and B. Deveaud-Pledran, Selective photoexcitation of confined exciton-polariton vortices, Phys. Rev. B **82**, 073303 (2010).
[26] F. Manni, K. G. Lagoudakis, T. Paraïso, R. Cerna, Y. Léger, T. C. H. Liew, I. Shelykh, A. V. Kavokin, F. Morier-Genoud, and B. Deveaud-Pledran, Spin-to-orbital angular momentum conversion in semiconductor microcavities, Phys. Rev. B **83**, 241307(R) (2011).
[27] M.-S. Kwon, B. Y. Oh, S.-H. Gong, J.-H. Kim, H. K. Kang, S. Kang, J. D. Song, H. Choi, and Y.-H. Cho, Direct transfer of light's orbital angular momentum onto a nonresonantly excited polariton superfluid, Phys. Rev. Lett. **122**, 045302 (2019).
[28] A. V. Yulin, A. V. Nalitov, and I. A. Shelykh, Spinning polariton vortices with magnetic field, Phys. Rev. B **101**, 104308 (2020).
[29] R. I. Kaitouni, O. El Daïf, A. Baas, M. Richard, T. Paraiso, P. Lugan, T. Guillet, F. Morier-Genoud, J. D. Ganière, J. L. Staehli, V. Savona, and B. Deveaud, Engineering the spatial confinement of exciton polaritons in semiconductors, Phys. Rev. B **74**, 155311 (2006).
[30] D. M. Myers, J. K. Wuenschell, B. Ozden, J. Beaumariage, D. W. Snoke, L. Pfeiffer, and K. West, Edge trapping of exciton-polariton condensates in etched pillars, Appl. Phys. Lett. **110**, 211104 (2017).
[31] E. Wertz, L. Ferrier, D. D. Solnyshkov, R. Johne, D. Sanvitto, A. Lemaître, I. Sagnes, R. Grousson, A. V. Kavokin, P. Senellart, G. Malpuech, and J. Bloch, Spontaneous formation and optical manipulation of extended polariton condensates, Nat. Phys. **6**, 860 (2010).
[32] E. S. Sedov, Y. G. Rubo, and A. V. Kavokin, Polariton polarization rectifier, Light: Sci. Appl. **8**, 79 (2019).
[33] J. Schmutzler, P. Lewandowski, M. Aßmann, D. Niemietz, S. Schumacher, M. Kamp, C. Schneider, S. Höfling, and M. Bayer, All-optical flow control of a polariton condensate using nonresonant excitation, Phys. Rev. B **91**, 195308 (2015).
[34] A. Askitopoulos, A. V. Nalitov, E. S. Sedov, L. Pickup, E. D. Cherotchenko, Z. Hatzopoulos, P. G. Savvidis, A. V. Kavokin, and P. G. Lagoudakis, All-optical quantum fluid spin beam splitter, Phys. Rev. B **97**, 235303 (2018).
[35] B. Berger, D. Schmidt, X. Ma, S. Schumacher, C. Schneider, S. Höfling, and M. Aßmann, Formation dynamics of exciton-polariton vortices created by nonresonant annular pumping, Phys. Rev. B **101**, 245309 (2020).
[36] E. Aladinskaia, R. Cherbunin, E. Sedov, A. Liubomirov, K. Kavokin, E. Khramtsov, M. Petrov, P. G. Savvidis, and A. Kavokin, Spatial quantization of exciton-polariton condensates in optically induced traps, Phys. Rev. B **107**, 045302 (2023).
[37] I. Gnusov, S. Harrison, S. Alyatkin, K. Sitnik, J. Töpfer, H. Sigurdsson, and P. Lagoudakis, Quantum vortex formation in the "rotating bucket" experiment with polariton condensates, Sci. Adv. **9**, eadd1299 (2023).
[38] Y. del Valle-Inclan Redondo, C. Schneider, S. Klembt, S. Hofling, S. Tarucha, and M. D. Fraser, Optically driven rotation of exciton–polariton condensates, Nano Lett. **23**, 4564 (2023).
[39] The following values of dimensional parameters in Eq. (2) correspond to the values of dimensionless parameters used for simulations. The effective polariton mass is $m^* = 5 \times 10^{-5} m_e$, where $m_e$ is the free-electron mass in vacuum, the polariton and reservoir excitons decay rates are $\Gamma_p = 0.06\text{ps}^{-1}$ and $\Gamma_r = 0.015\text{ps}^{-1}$, respectively, and the stimulated scattering rate

is $g_1 = 0.006\text{ps}^{-1}\,\mu\text{m}^2$. The polariton-polariton and polariton-exciton scattering constants are estimated as $H \approx 1.18\,\mu\text{eV}\,\mu\text{m}^2$ and $\hbar g_2 \approx 12\,\mu\text{eV}\,\mu\text{m}^2$, respectively, the nonlinear losses are $\tilde{H} \approx 0.1\text{ns}^{-1}\,\mu\text{m}^2$.

[40] A. V. Yulin, A. S. Desyatnikov, and E. A. Ostrovskaya, Spontaneous formation and synchronization of vortex modes in optically induced traps for exciton-polariton condensates, Phys. Rev. B **94**, 134310 (2016).